Research article

A high accuracy measurement method based on vortex polar axis rotation phase-shifting interferometry (VPAR-PSI)

Zhisong Li [a], Jiaxing Sun [a], Xiao Xu [a], Yu Chen [b,*], Honglei Hu [a]

[a] *College of Machine, Shanghai Dianji University, Shanghai, 201306, PR China*
[b] *College of Science, Donghua University, Shanghai, 201620, PR China*

ARTICLE INFO

ABSTRACT

For higher precision phase shift measurement, based on the characteristics of vortex beam, the manuscript introduces phase shift directly through the polar axis rotation of the vortex beam. Compared to traditional grey-scale modulation, the proposed VPAR-PSI method introduces a phase-shifting directly instead of changing the grey-scale, which not only can largely reduce the deviation caused by traditional PSI phase modulation via grey-scale change, but also can effectively avoid the non-linearity between grey-scale and phase of traditional PSI. For verifying the effectiveness of the method proposed in this manuscript, a simulation experiment, sample experiment, and VPAR-PSI and PSI comparison experiment were conducted. The results show that the proposed VPAR-PSI has a high phase-shifting and demodulation accuracy, and can be well implemented to measurement of optical components. The comparative experimental show that compared to conventional PSI, the measurement results of VPAR-PSI have smaller envelope values (mean envelope reduction of 1.4202λ), smaller RMS and standard deviation (the values decreased by 0.3515, 0.3067, and the percentage decreases were 59.69%, 59.71% respectively), proving that the VPAR-PSI technique are more accurate and stable.

© 2020 Published by Elsevier Ltd. Selection and/or peer-review under responsibility of Global Science and Technology Forum Pte Ltd.

1. Introduction

In the 1980s, phase shift interferometry (PSI) was introduced by Bruning et al. [1] and then applied to the area of optical interferometry. The basic theory of the PSI method is to recover the wavefront phase information by phase-demodulation of the image sequence (at least three frames), thus achieving a 3D reconstruction of the target's surface form [2–4]. A series of advantages including simple in construction, full-field sensing, contactless, precision, high sensitivity, non-damage and a high speed of measurement are offered by PSI. With 40 years of advancements, PSI now has steadily replaced conventional touch detection techniques as an essential tool for a vast range of measurement in a variety of applications [5,6]. The typical implementation of PSI is to create a series of interferometric images by introducing a predetermined phase shift (or optical range) in the reference (or measurement) path of the interferometric optical path, resulting in a constant phase shift between the reference and measurement paths, thus obtaining a sequence of interferometric images with a constant phase shift. The interferometric image sequence with a certain phase-difference is captured by the electro-optical sensor, and the computer can extract information about the wavefront phase distribution by calculating

---

* Corresponding author.
  E-mail address: lizs@sdju.edu.cn (Y. Chen).

these image sequences [7]. Additionally, pre-set phase shifts are typically produced by a phase shifter (e.g., PZT, wavelength tuning laser, etc.) in the PSI Multi-Step Phase Shift technique [8,9].

In the area of methods for calculating PSI phase-shifting demodulation, plenty of surveys were conducted by a large number of scholars at both domestic and overseas in recent years. During the initial stage of research, classes of phase shifting algorithms such as 4-step, 5-step, 6-step and N-step phase shifting algorithms have been introduced [10–12]. Over recent years, the randomized iterative least squares fitting algorithm (AIA), the principal component analysis (PCA) method, the wavelength modulation algorithm and the 2-step phase shift algorithm based on the G. Schmidt orthogonal transform have been further proposed [13–15]. All of the above phase demodulation algorithms have been developed to a higher level in terms of demodulation accuracy, speed and robustness. One of the important prerequisites for the accurate PSI phase demodulation results described above is on the condition that the phase-shifting operation is very precise and stable. Yet, because in practice PSI is used to phase shift by means of phase shifters (e.g. piezoelectric ceramics (PZT), a wavelength-tuned laser, and so on), PSI outcomes are constrained and limited by a number of elements, resulting in the following problems which inevitably arise in its engineering applications [16–18]. 1) Traditional PSI technology is limited to a large extent by the characteristics of the phase shifter itself, which has a long phase shift period and low accuracy; 2) Traditional PSI technique is multi-step phase shifting technique in the time domain with long phase modulation periods (e.g., nine-step phase shifting techniques), which are sensitive to phase shifter action and vibration interference from the external environment, and cannot meet the needs of dynamic environments and high-precision measurements; 3) Traditional PSI is generally a modulation in the form of wavefront phase consistent, which does not enable accurate phase shifting at the pixel level. This means that current PSI techniques not only require a very stable measurement environment, but also the cost of achieving high precision interferometry is very high (requiring vibration resistant platforms etc.). Therefore, the development of high precision PSI technology and further research is necessary for PSI to reduce the environmental requirements and achieve high precision measurements.

The swirling beam, also known as an optical swirl, which is a swirling distributed light field with phase singularities, is one where the light shows a ring-like distribution with a black spot in the center [19,20]. Swirl beams have also been called OAM beams due to the fact that they carried orbital angular momentum (OAM) [21]. Angular momentum of an optical orbit theoretically provides an infinite multi-dimensional and orthogonal basis for message encoding [22] and optical transmission [23–25]. On the basis of its unique interference and diffraction properties, investigations into the optical transmission receiving end of OAM detection are underway [26–28]. Scroll light is also used effectively in other areas, such as in optical entrapment [29], ultra-resolution imaging for microscopes [30] and metrology [31,32]. In the case of PSI technology, the angular momentum characteristics of the orbital beam of an eddy current beam will generate area-wide, pixel-scale phase-modulation, which means greater phase resolution. Within the area of PSI, the swirl light beam may be created with a spatial light modulator (SLM), which operates at a very accurate stage shift [33–35]. With a coupling of scroll light beam phase displacement and phase unpacking technique, contactless, higher resolutions and a wider range of metrology solutions such as micro-deformations of materials, micro-displacement and optical device shapes can be realized [36]. There is a new methodology presented by Sun and others for the measurement of in-plane movements of bodies via the speckle interference principle by means of applying optical swirl phase transfers to spot measurements [37]. Additionally, Zhang and others took an oval vortex lens into phase-shifted image-planar digital holography and tested the multi-planar focal points of the target and the baroscopic lens [38]. In parallel, a 3-dimensional index of refraction of the special fibers was measured by Wang and others with the aid of an eddy current transmission numerical holography mass spectrometer [39]. On the subject of interface metrology, Masajada and others using an optical swirl interferometer to examine the surface by scanning the texture of the material with a focused swirl stream and a novel approach to inspect in-depth nanostructures fabricated in transparent medias has been reported [40]. A cross-path interferometer working upon the phase-singularity of the optical swirl stream has been described by Serrano-Trujillo and others, this interferometer can reach a mean surface depth of 179 nm [41]. In spite of the existing use of swirl interference to the area of PSI, the present PSI of swirl light is created by indirect implementation of phase modulation via a grey-level picture to the SLM [42]. Such a method involves not only a significant error in phase-shift owing to the phase shift introducing by a grey-scale modulation, but it also fails to overcome the uncertainty of non-linearity between optical brightness and phase [43–45].

In order to achieve high precision phase shift measurements, based on the characteristics of vortex light, this paper proposes a method to introduce phase-shift directly by vortex polar axis rotation of the vortex light. Compared to existing PSI grey-scale modulation methods, the proposed vortex polar axis rotation Phase-Shifting interferometry (VPAR-PSI) measurement method not only significantly reduces the error caused by grey-scale changes, but also effectively avoids the non-linearity problem between grey-scale and phase calculations. The proposed VPAR-PSI measurement process in this manuscript is as follows. Firstly, a high precision planar reference mirror is selected to perform a four-step phase shift (0, $\pi/2$, π, $3\pi/2$) using a polar axis transformation, and the phase distribution of the reference mirror is calculated to obtain information on its initial spiral phase distribution. Secondly, the plane mirror is replaced with the element to be measured, and the same polar axis transformation is used to achieve a four-step phase shift, after which the sum of the phase information including the element to be measured and the initial spiral phase is obtained. Finally, a difference algorithm is used to obtain wavefront phase information representing the profile of the component to be measured.

2. Method and theory

2.1. Principle of vortex light

For traditional PSI, the phase shift component is used to achieve full and consistent modulation of the phase, which means that if the resolution of the interferometric image is X*Y (X is number of rows, Y is number of columns), the phase shift δ_n at any point (x, y) on the CCD is the same after phase modulation. The optical expression for the point (x, y) can be written as equation (1).

$$I_n(x,y) = a(x,y) + b(x,y)cos(\varphi(x,y) + \delta_n), n = 1, 2, ...N \tag{1}$$

where, $a(x,y)$ represents the background light intensity, $b(x,y)$ represents the modulation system, $\varphi(x, y)$ represents the phase to be measured, and δ_n is the step phase shift. n and N represent the current frames, and the total number of images captured, respectively.

For vortex beam, it is a dark hollow beam with a continuous spiral phase, which shows a vortex-like anisotropic polarization distribution in the cross-section. The phase distribution of the vortex beam is determined by the phase factor $exp(l\varphi)$. After phase modulation of the vortex light, the phase shift at any point on the CCD is directly related to $l\theta_n(x.y)$. If the phase shift at any point on the CCD after phase modulation is $l\theta_n(x,y)$, the optical expression can be written as equation (2).

$$I_n(x,y) = a(x,y) + b(x,y)cos(\varphi(x,y) + l\theta_n(x,y)), n = 1, 2, ...N \tag{2}$$

where, $a(x,y)$, $b(x,y)$ represent the background light intensity, contrast, $\varphi(x,y)$ represents the phase to be measured. n and N represent the current number of frames, the total number of frames acquired, respectively. l is the topological charge, and θ represents the polar angle.

Comparing equations (1) and (2) it can be seen that traditional PSI phase shifting techniques introduce step phase shifts according to the amount of phase shift δ_n. In contrast, vortex light is based on its unique spiral phase term $exp(il\theta)$ to achieve pre-determined phase modulation. A comparison of the traditional PSI phase-shifting and vortex phase-shifting introduction methods is shown in Fig. 1.

2.2. Vortex polar axis rotation phase-shifting

1) Phase difference between two points under polar coordinate system

As can be seen from the description above, the phase information of PSI technique is characterized by the pixel greyscale of the CCD, which means that the spatial position is defined by pixel coordinates of the CCD, i.e., a Cartesian coordinate system in the plane. However, for vortex beam, the spiral phase value is determined by the topological charge and the polar angle together, so the vortex beam phase is expressed in a polar coordinate system. According to the transformation relationship between the Cartesian and polar coordinate systems, if the Cartesian coordinate origin (x_0, y_0) coincides with the polar coordinate origin, the polar coordinates corresponding to the pixel of the point (x,y) under the Cartesian coordinate system can be written as equation (3).

$$\begin{cases} r = \sqrt{(x-x_0)^2 + (y-y_0)^2} \\ \theta = \tan^{-1}((y-y_0)/(x-x_0)) \end{cases} \tag{3}$$

where, r denotes the polar diameter and θ denotes the pole angle.

From the above equation, the phase of the vortex beam varies periodically with the spatial coordinate distribution of the phase. Assuming that the topological charge l is equal to 1 and the vortex beam is drawn with the origin (x_0, y_0) as the centre of the circle and the number of pixels as the radius, the vortex beam is a circular loop with a phase gradient which changes from 0 to 2π. And the schematic diagram is shown in Fig. 2 (a).

In the polar coordinate system, there exists a pixel point A (x_A, y_A) with spiral phase θ_A. Under the condition that the size of polar diameter is constant, along clockwise direction, there exists a point B (x_B, y_B) with phase difference α (shown in Fig. 2 (middle)). According to the coordinate transformation relation pixel B coordinates can be expressed as equation (4).
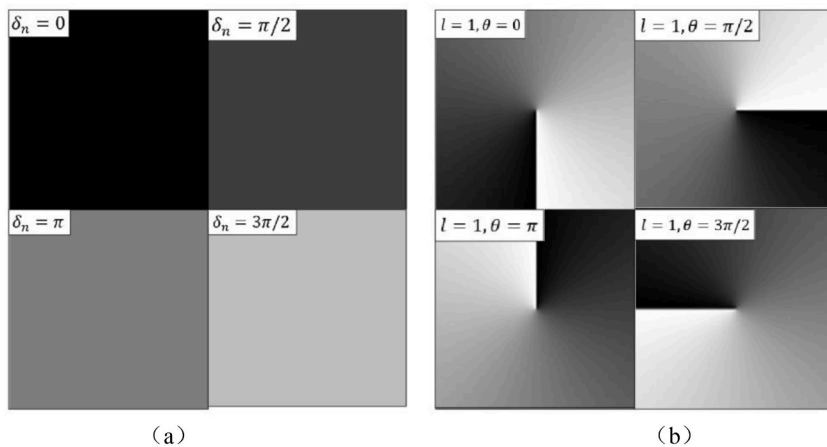

(a)   (b)

Fig. 1. Schematic diagram of traditional PSI and vortex phase shift; (a) schematic diagram of traditional PSI phase shift; (b) schematic diagram of vortex phase shift.
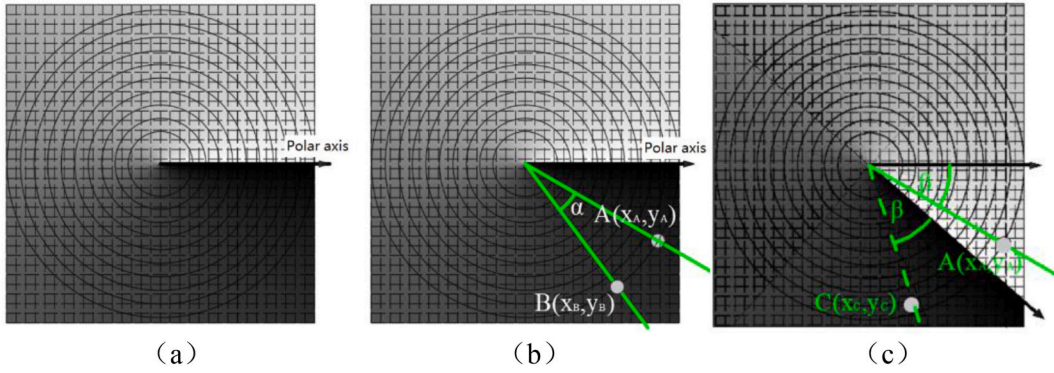
Fig. 2. Schematic diagram of polar-axis rotation phase modulation of vortex beam; (a) schematic diagram of vortex beam phase distribution; (b) schematic diagram of vortex beam phase difference; (c) schematic diagram of vortex beam polar-axis rotation transfer phase principle.

$$\begin{cases} x_B = r_0 \cdot \cos(\theta_A + \alpha) \\ y_B = r_0 \cdot \sin(\theta_A + \alpha) \end{cases} \tag{4}$$

According to the cosine theorem, the distance between pixel points A and B can be written as equation (5).

$$L_{AB} = \sqrt{2r_0^2 - 2r_0^2 \cos \alpha}$$
$$= \sqrt{x_A^2 + y_A^2 + x_B^2 + y_B^2 - 2\sqrt{(x_A^2 + y_A^2)(x_B^2 + y_B^2)}\cos \alpha} \tag{5}$$

2) Principle of polar-axis rotation phase shift

If the phase shift of the vortex beam is achieved by rotation of the polar axis in the polar co-ordinate system, the first step is to define the constraint relationship between the rotation angle of polar axis and the phase shift of vortex beam. Assuming that the vortex polar axis is rotated by an angle β along the counter clockwise direction (as shown in Fig. 2 (b)), and that pixel A moves to pixel C (x_C, y_C), and pixel C with a spiral phase θ_C. A relationship exists as shown in equation (6) below.

$$\begin{cases} x_C = r_0 \cdot \cos(\theta_C + \beta) \\ y_C = r_0 \cdot \sin(\theta_C + \beta) \end{cases} (\theta_C = \theta_A) \tag{6}$$

According to the cosine theorem, the distance between pixel A and C can be expressed as equation (7).

$$L_{AC} = \sqrt{2r_0^2 - 2r_0^2 \cos \beta}$$
$$= \sqrt{x_A^2 + y_A^2 + x_C^2 + y_C^2 - 2\sqrt{(x_A^2 + y_A^2)(x_C^2 + y_C^2)}\cos \beta} \tag{7}$$

From Eqs. (3)–(7), when the vortex beam shift phase η is equal to the polar axis rotation angle ξ, there exists a relationship as shown in equation (8).

$$\begin{cases} x_B = x_C = r_0 \cdot \cos(\eta + \xi) \\ y_B = y_C = r_0 \cdot \sin(\eta + \xi) \\ L_{AB} = L_{AC} = \sqrt{2r_0^2 - 2r_0^2 \cos \xi} \end{cases} (\theta_A = \theta_B = \eta, \alpha = \beta = \xi) \tag{8}$$

From equation (8), it can be seen that pixel C overlaps with pixel B when the vortex beam shift phase is equal to the angle of rotation of the polar coordinate axis. This means that phase modulation can be achieved by rotation of the vortex beam polar axis, and the polar axis rotation angle ξ is exactly equal to the vortex beam phase shift η when the topological charge $l = 1$.

2.3. VPAR-PSI phase demodulation method

Using the vortex phase modulation method described in the above section, the polar axis is rotated by 0, $\pi/2$, π, $3\pi/2$, and four interferometric images are acquired respectively, the interferometric image light intensity can be noted as.

$$\begin{cases} I_{s,0}(x,y) = a(x,y) + b(x,y)cos(\Delta\varphi(x,y) + \theta_0(x,y)) \\ I_{s,1}(x,y) = a(x,y) + b(x,y)cos(\Delta\varphi(x,y) + \theta_0(x,y) + \pi/2) \\ I_{s,2}(x,y) = a(x,y) + b(x,y)cos(\Delta\varphi(x,y) + \theta_0(x,y) + \pi) \\ I_{s,3}(x,y) = a(x,y) + b(x,y)cos(\Delta\varphi(x,y) + \theta_0(x,y) + 3\pi/2) \end{cases} \tag{9}$$

where, $\theta_0(x,y)$ represents the spiral phase distribution, and $\Delta\varphi(x,y)$ is the phase of the wave front introduced by the standard mirror. In the actual measurement process, the background light intensity term $a(x,y)$ and the contrast $b(x,y)$ are invariant.

Based on the trigonometric relationship, equation (9) can be transformed as equation (10).

$$\frac{I_{s,3}(x,y) - I_{s,1}(x,y)}{I_{s,0}(x,y) - I_{s,2}(x,y)} = \frac{sin[\Delta\varphi_s(x,y) + \theta_0(x,y)]}{cos[\Delta\varphi_s(x,y) + \theta_0(x,y)]} = tan[\Delta\varphi(x,y) + \theta_0(x,y)] \tag{10}$$

If a high precision plane mirror is used for the initial phase calibration. The initial spiral phase $\theta_0(x,y)$ can be expressed as equation (11).

$$R_1 = \Delta\varphi(x,y) + \theta_0(x,y) \cong \theta_0(x,y) = arc\,tan\left[\frac{I_{s,3}(x,y) - I_{s,1}(x,y)}{I_{s,0}(x,y) - I_{s,2}(x,y)}\right] \tag{11}$$

where, R_1 represents the wrapped phase of a standard plane mirror. Similarly, the actual wrapped phase can be written as equation (12).

$$R_2 = \Delta\varphi(x,y) + \theta_1(x,y) = arc\,tan\left[\frac{I_3(x,y) - I_1(x,y)}{I_0(x,y) - I_2(x,y)}\right] \tag{12}$$

where, R_2 denotes the actual wrapped phase, $\Delta\varphi(x,y)$ is the phase of the lens to be measured; $\theta_1(x,y)$ is the initial spiral phase.

According to the phase distributions R_1 and R_2 obtained from equations (11) and (12), after unwrapping and Zernike fitting to eliminate the tilt term, the accurate initial phase distribution $R_{1\ zernike}$ of the spiral beam and the actual test phase distribution $R_{2\ zernike}$ can be obtained respectively. Finally, the phase distribution $\Delta\varphi(x,y)$ of the test mirror can be written as equation (13).

$$\Delta\varphi(x,y) = R_{2\ zernike} - R_{1\ zernike}$$
$$= \left(arc\,tan\left[\frac{I_3(x,y) - I_1(x,y)}{I_0(x,y) - I_2(x,y)}\right]\right)_{zernike} - \left(arc\,tan\left[\frac{I_{s,3}(x,y) - I_{s,1}(x,y)}{I_{s,0}(x,y) - I_{s,2}(x,y)}\right]\right)_{zernike} \tag{13}$$

Where, $\Delta\varphi(x,y)$ represents the phase distribution of the lens to be measured after unwrapping.

2.4. VPAR-PSI testing process

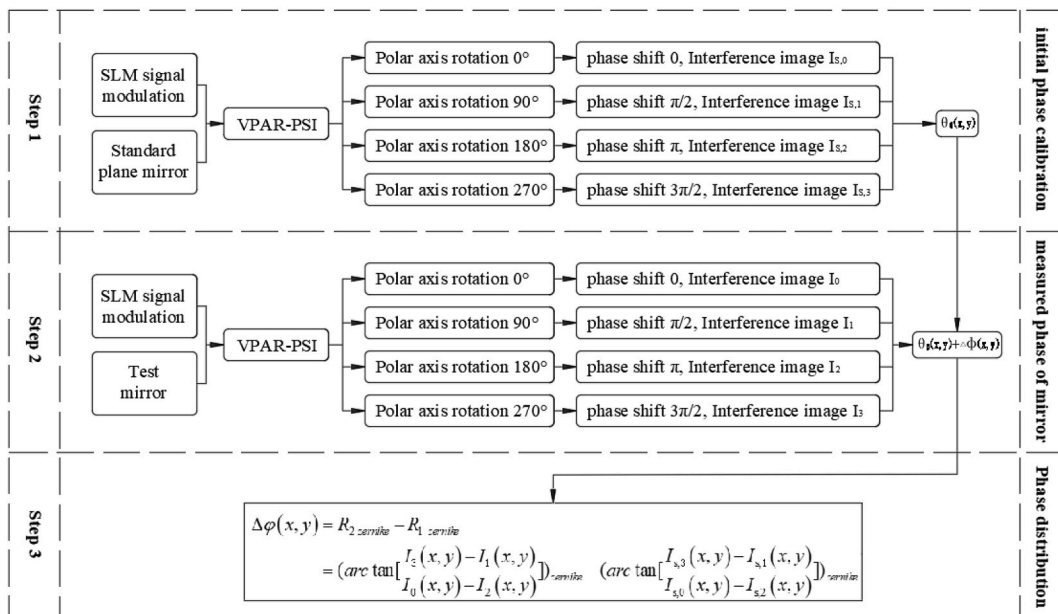The detection flow of our proposed VPAR-PSI method is shown in Fig. 3.

Fig. 3. Flow chart of vortex polar axis rotation Phase-Shifting interferometry (VPAR-PSI).

3. Measuring equipment

To verify the feasibility and effectiveness of the vortex phase transfer method proposed above, an interferometric system which enables vortex optical polar axial rotation to transfer phases is constructed. Fig. 4 (above) shows the schematic diagram of vortex light interference system designed in this manuscript, which uses a Thayman-Green interference optical path. The interference system uses a laser (50mw, 532 nm) to project laser light, then divides it into a reference light and an object light after passing through attenuator, polarizer (polarizer is to ensure that the polarization direction is consistent with the direction of the long axis of the liquid crystal of LC-SLM) and beam expander. The object light reaches the surface of CCD (Basler pixel size 3.55 μm × 3.55 μm, resolution of 2448 × 2048 pixels, sampling rate 25 fps) after passing through a beam expander, test mirror, beam splitter and filter. The reference light is reflected by a liquid crystal spatial light modulator (LC-SLM, resolution 1920 × 1152, LCD spatial light modulator response speed 833 Hz) and then reaches the CCD surface after passing through a beam expander, half-reflective half-lens (BS) and filter. Ultimately, the object light and the reference light form a stable interference on the CCD surface.

In addition, it should be noted that this manuscript uses LC-SLM to generate the vortex beam on the reference optical path and to realize the spin-transfer phase of the vortex beam.

4. Experimental verification and analysis

To verify the feasibility and effectiveness of the proposed vortex beam shift in this paper, three separate experiments were conducted in this manuscript as follows. Simulation tests to verify the feasibility of vortex optical phase shifting, experimental verification of the feasibility of vortex optical phase shifting, and PSI versus VPAR-PSI detection effectiveness test.

4.1. Simulation tests

Simulation experiments are conducted in this paper. The simulation experiment flow includes, vortex light wavefront phase calibration, test mirror wavefront phase measurement, and test mirror wavefront phase measurement with noise.

1) Vortex light wavefront phase calibration

Before interferometric measurement with VPAR-PSI, the wavefront phase distribution of the vortex light needs to be obtained, therefore a vortex light wavefront phase calibration is required. To facilitate the observation of fringes, the objective light is set to a periodic phase distribution along the horizontal (number of periods T = 6, and the number of T can be obtained by counting the number of light and dark fringes), which represents a standard plane mirror with a certain tilt. The reference light is set to a vortex light with a topological charge equal to 1 and the polar axis along the positive x-axis. After the reference light interferes with the object light, the simulated interference image (image size is 200pixel* 200pixel) is shown in Fig. 5.

Based on the above VPAR-PSI simulation image, phase calculations were performed and experimental results were obtained as
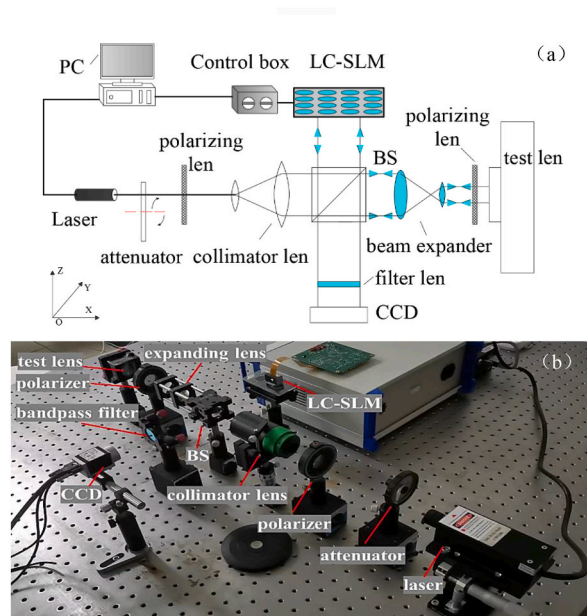

Fig. 4. VPAR-PSI system; (a) principle of the VPAR-PSI system; (b) physical drawing of the VPAR-PSI system.
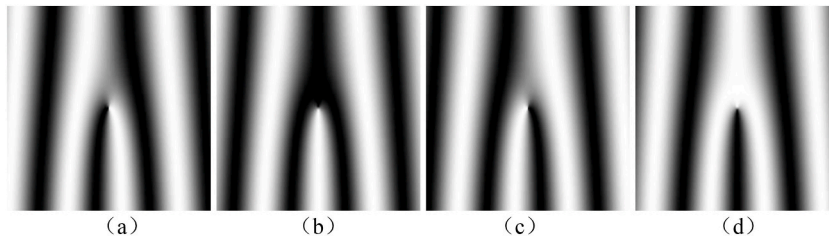
Fig. 5. VPAR-PSI simulation image (polar axis rotation angles: 0 (a), 90° (b), 180° (c), 270° (d).

shown in Fig. 6. Where, Fig. 6 (a) shows the wrapped phase distribution, Fig. 6 (b) shows the unwrapped phase distribution, and Fig. 6 (c) shows the phase distribution after eliminating the tilt term.

From the simulated experimental data in Fig. 6, it can be seen that the wavefront phase after eliminating the tilt term is consistent with the initial wavefront phase distribution of the vortex beam, thus proving the feasibility of the phase shift method proposed in this manuscript.

2) Error analysis of simulation tests

In the same way as above, the vortex light polar axis is rotated counter clockwise by 0, $\pi/2$, π, $3\pi/2$ and interferes with the object light (which is set to a periodic phase distribution along the horizontal direction (number of periods T = 7)) to obtain simulated interference images. The obtained phase distribution data are shown in Fig. 7.

According to the method proposed in this manuscript, the actual shape of the plane mirror is obtained by eliminating the phase of the wave front, and the results is shown in Fig. 8 (a). In addition, in order to observe the phase distribution, the phase distribution of 10 rows and columns (row: 96–105, column: 96–105) in the center of the phase map were extracted and a phase distribution comparison was constructed, and the results are shown in Fig. 8 (b) and (c).

From the above, it is clear that after removing the tilt factor, the plane mirror should be an ideal plane. However, as can be seen from Fig. 8, there is a deviation in the simulation results from the ideal plane. In order to further quantify the accuracy of the proposed phase shift method, the mean, standard deviation (SD) and root mean square (RMS) for each row and column were calculated and the results are shown in Fig. 9.

As can be seen from Fig. 9, the mean and RMS values of the phase demodulation errors for each row and column of pixels are below $8*10^{-13}$, and the maximum and minimum standard deviations are $0.18*10^{-13}$ and $0.12*10^{-13}$ respectively. This means that the proposed VPAR-PSI method in this paper has high phase demodulation accuracy and good consistency.

3) Simulation experiments with noise

To further evaluate the phase-shifting effect of VPAR-PSI under realistic environments, simulations of phase-shifting measurements were carried out after adding random noise (±0.5 rad of random phase variation) to the interferometric images. The phase shift operation was carried out with the same approach as above, and the interference image obtained is shown in Fig. 10.

According to obtained interference images a phase demodulation process was performed and the obtained phase distribution results are shown in Fig. 11.

In order to analyses and verify the accuracy and stability of the VPAR-PSI proposed in this paper, eight sets of simulation test experiments with noise factors were conducted. According to the data of multiple simulation experiments, the maximum and minimum values of its phase distribution are calculated respectively, and the calculation results are shown in Fig. 12 (a). In addition, according to the range of the set noise, the percentage of elements in the phase distribution where the data exceeds the maximum value is counted
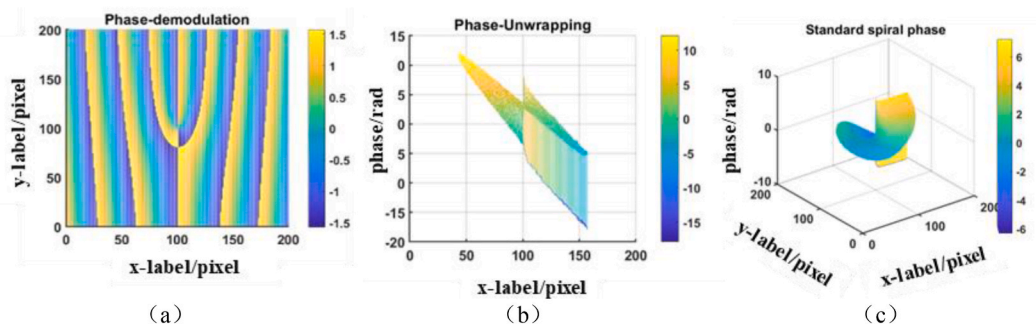

Fig. 6. Simulation experimental data for the initial phase calibration of VPAR-PSI; (a) wavefront phase map, (b) wavefront unwrapped phase map, (c) wavefront phase map after eliminating tilt term.
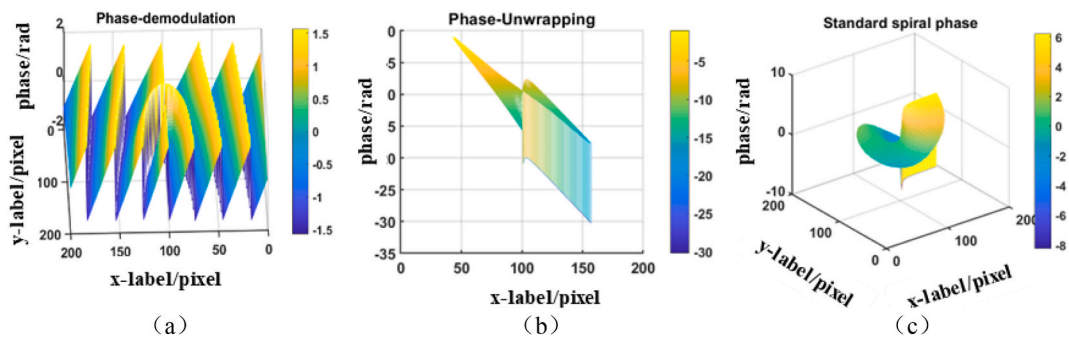
Fig. 7. Phase distribution data obtained from vortex interference phase-shift phase extraction; (a) phase map, (b) unwrapped phase map, (c) wavefront phase map after eliminating tilt term.
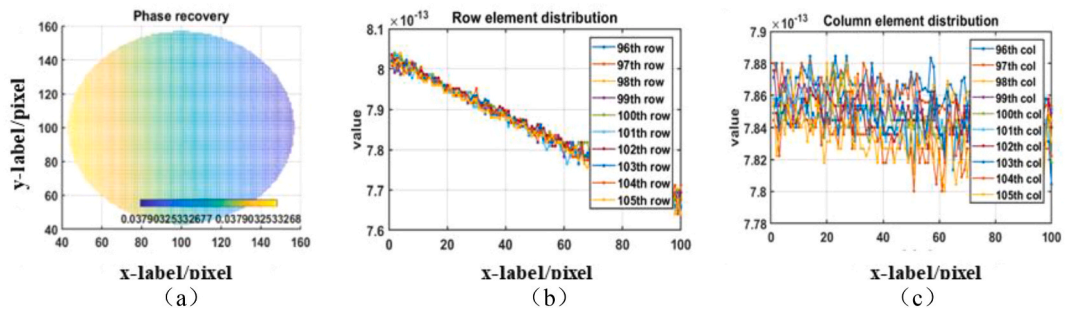

Fig. 8. Plane mirror shaped phase distribution data; (a) plane mirror shaped phase distribution, (b) phase distribution information for rows 96–105, (c) phase distribution information for columns 96–105.
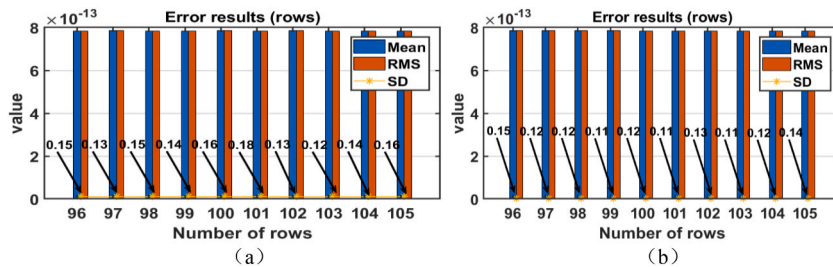

Fig. 9. Evaluation of the results of the phase distribution of the plane mirror; (a) mean, SD and RMS of each row, (b) mean, SD and RMS of each column.
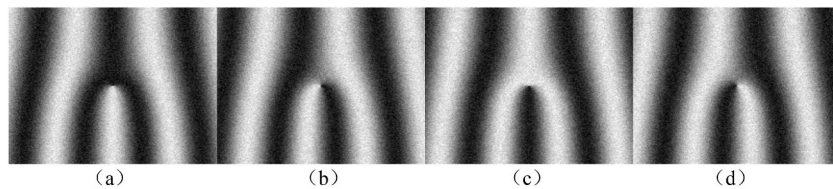
Fig. 10. Simulated interference images with noise (polar axis rotation angles: 0 (a), 90° (b), 180° (c), 270° (d).

and the results are shown in Fig. 12 (b).

From the above experimental data, it can be seen that the maximum value is 1.3617 rad, the minimum value is 1.2219 rad and the mean value is 1.2824 rad in the eight groups of phase distribution information; and the percentage of pixels above and below the preset error range is 3.7% and 2.6% respectively. As a result, the average error of the proposed VPAR-PSI method is 0.031 rad, and the error pixel percentage is 3.1% under a condition of random interference. This proves that the proposed VPAR-PSI method has good demodulation accuracy and repeatable measurement stability even for interferometric images with interference.
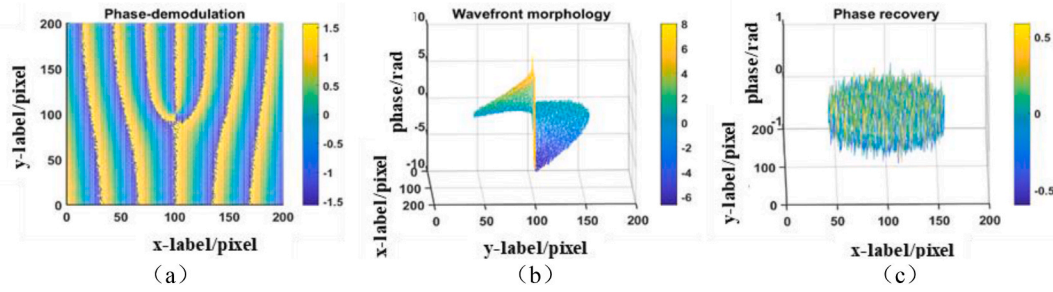
Fig. 11. Plane mirror wavefront phase distribution data with noise; (a) phase map after phase extraction, (b) phase map after removal of the tilt term; (c) wavefront phase distribution for the plane mirror shape.
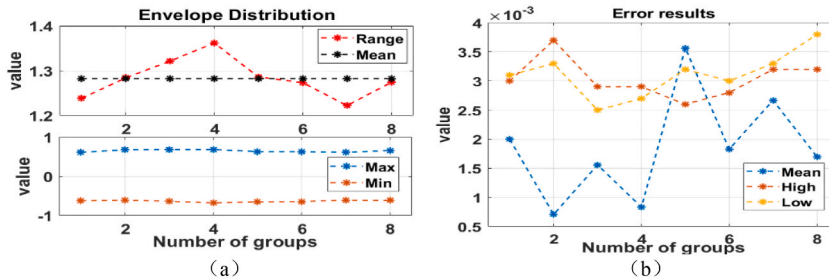

Fig. 12. Simulated experimental phase distribution data from multiple sets; (a) maximum and minimum values of the phase distribution; (b) percentage of elements above and below the preset noise and the average value of the phase distribution data.

4.2. Sample measurement experiments

To verify the practical detection effectiveness of the proposed VPAR-PSI method, the samples were selected for shape detection using the experimental system built above. Following the process above, the vortex light phase calibration was performed. According to the method above, after performing phase shift, the acquired interferometric images are shown in Fig. 13.

Based on the interferometric image shown in Fig. 13, the vortex light wavefront phase calibration was performed. The obtained vortex light wavefront phase information is shown in Fig. 14.

Based on the obtained vortex wavefront phase information shown in Fig. 14, three times measurement of high precision plane mirror surfaces is carried out and the results are shown in Fig. 15.

To verify the detection accuracy of the VPAR-PSI method, multiple repetitive detection experiments (16 times) were carried out, and the information from central region of phase map was extracted separately for comparative. The maximum, minimum, mean, RMS and standard deviation of the measurement error were counted, and the percentage of pixels with an error of less than 0.1 rad were counted, and the results were calculated as shown in Fig. 16.

From the experimental data in Fig. 16, it can be seen that the mean error of phase demodulation is 0.19 rad, and the mean values of standard deviation and RMS are 0.14 and 0.24 respectively. This proves that the VPAR-PSI method proposed in this manuscript not only has high phase demodulation accuracy, but also low dispersion and high convergence.

2) Test 2: spherical mirror measurement

Selecting the spherical mirror sample, a number of phase shifts of 0, $\pi/2$, π, and $3\pi/2$ were introduced respectively by polar axis rotation using the VPAR-PSI method proposed in this paper. The obtained interference images are shown in Fig. 17.

In the same way, the spherical mirror shape is calculated. The results of the spherical shape measurements are shown in Fig. 18.

In the same way as above, in order to quantitatively analyses the phase measurement accuracy of the proposed method, 16 times repeated tests were carried out separately. Based on the results of the 16 times of testing, the phase distribution in the central region of the image was extracted separately for data comparison and analysis. The maximum value, minimum value, standard deviation, RMS value and envelope values (calculated from maximum and minimum values) were calculated for each of the 16 sets of data. The results are shown in Fig. 19.

From the data of 16 times of experiments shown in Fig. 19 (a), it can be seen that the measurement deviation of the results is 0.3511 and the mean values of RMS and standard deviation are 0.0901 and 0.0903. Similarly, from the data of the 16 times experiments shown in Fig. 19 (b), the measurement deviation of the test results is 0.3380 and the mean values of RMS and standard deviation are 0.0927 and 0.0956. As a result, the VPAR-PSI method proposed in this paper is able to achieve a high level of measurement accuracy and stability in practical applications.
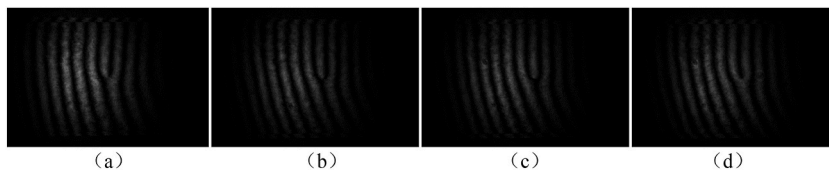
Fig. 13. Interferometric images obtained by polar axis rotation of the vortex light (polar axis rotation angles: 0 (a), 90° (b), 180° (c), 270° (d), respectively).
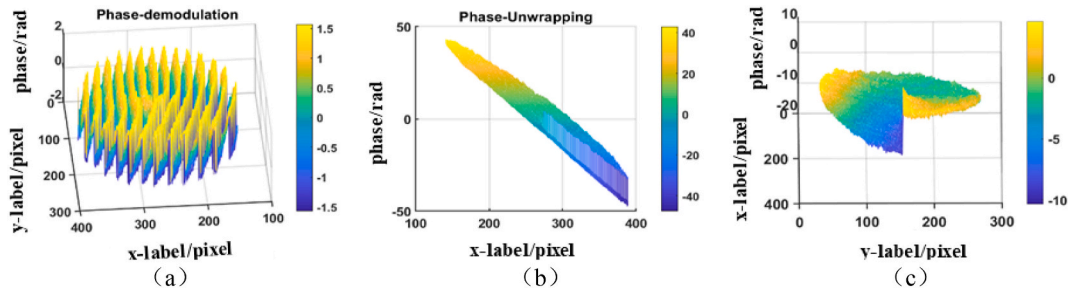

Fig. 14. Vortex beam wavefront phase calibration results; (a) wrapped phase map, (b) unwrapped phase map, (c) vortex beam wavefront phase map after elimination of tilt term.

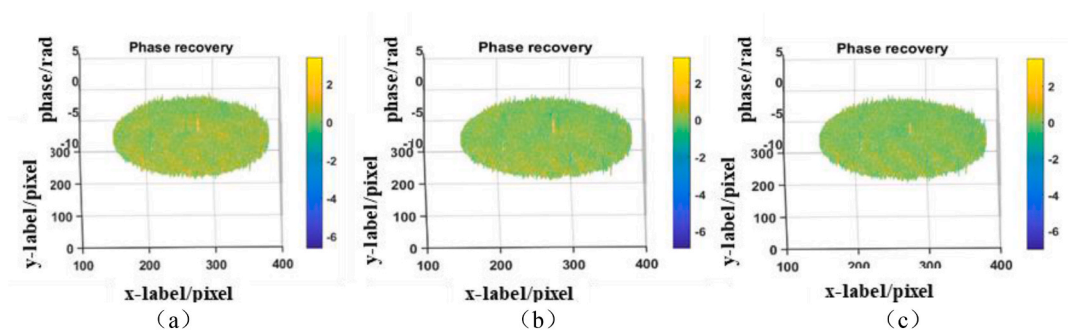1) Experiment 1: Flat mirror shape detection

Fig. 15. Results of three times measurement of high precision plane mirror surfaces; (a) first time, (b) second time, (c) third time.
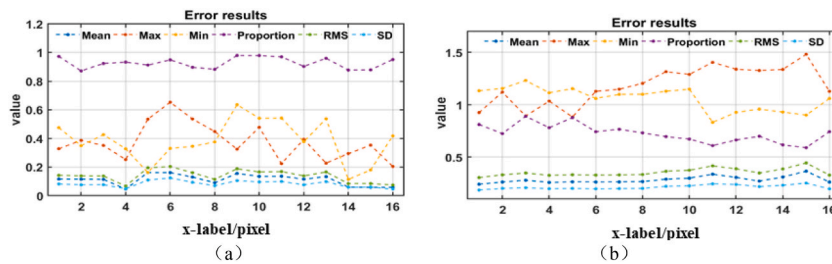

Fig. 16. Error analysis of the results of the plane mirror surface; (a) results of the data error analysis; (b) results of the data error analysis.

4.3. VPAR-PSI and PSI comparison experiment

In order to contrast the effectiveness of proposed VPAR-PSI with the traditional PSI phase shift technique, a spherical mirror was selected for comparison experiments. First, according to the principle of traditional PSI phase-shifting interference technique [22], the obtained interferogram, unwrapped phase map, wrapped phase map, and wrapped phase map with tilt removed are shown in Figs. 20 and 21 respectively.

The results of spherical mirror shape measurements based on VPAR-PSI with PSI phase shift technique are shown in Fig. 22.
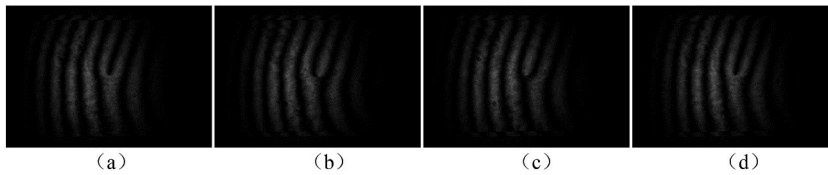
Fig. 17. VPAR-PSI phase-shifted (axis rotation angles: 0 (a), 90° (b), 180° (c), 270° (d), respectively) interference images.
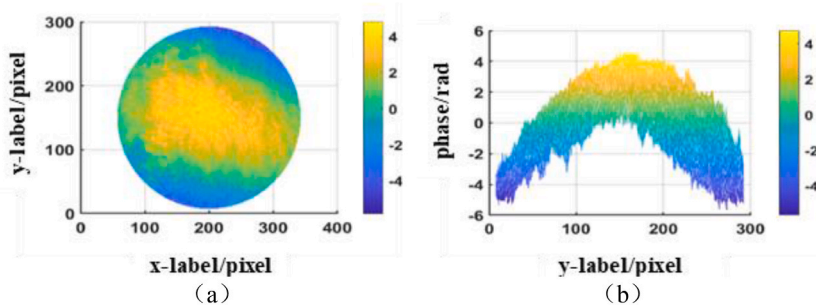

Fig. 18. Results of spherical mirror shape measurements; (a) x-y direction view; (b) y-z direction view.
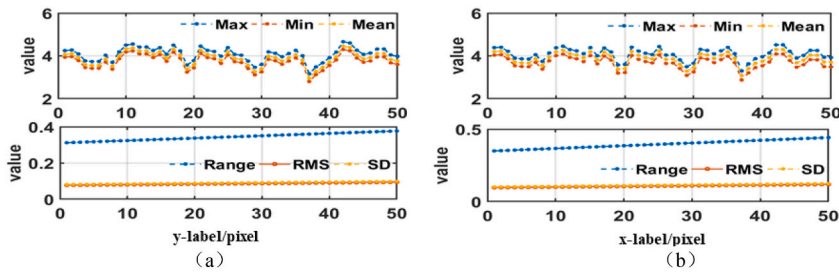

Fig. 19. Analysis of data results for spherical mirror shape; (a) Fig. 18 (a) Analysis of data results; (b) Fig. 18 (b) Analysis of data results.
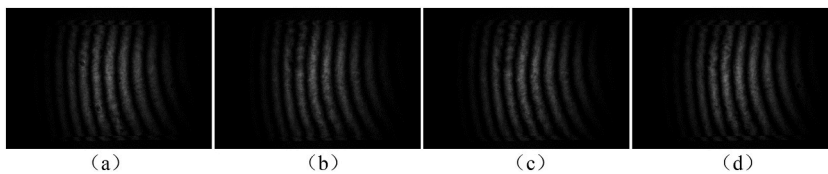

Fig. 20. Interference images from traditional PSI phase shifts (from left to right: 0 (a), 90° (b), 180° (c), 270° (d)).

To further compare the measurement of VPAR-PSI with that of PSI, the data in row 150 and column 200 of Fig. 22 were taken and compared respectively, and the results are shown in Fig. 23.

As can be seen from Fig. 23, for same conditions, the PSI has a more implausible "stepped" distribution in the row and column directions than the data measured by VPAR-PSI (because the lens surface shape distribution is continuous and smooth). This proves that the traditional PSI technique introduces more phase errors in the process of phase shifting, resulting in a large deviation between the real phase shift and the preset value, which ultimately leads to inaccurate phase demodulation.

To further accurately compare and quantitatively analyses the measurement effects of VPAR-PSI and PSI, the rows 135–165 and columns 185–215 of Fig. 22 were taken for statistical calculations respectively. Their maximum, minimum, envelope, variance, standard deviation and mean values of each row were calculated and the final measurement results are shown in Fig. 24.

According to Fig. 24 the mean values of each parameter were calculated and the results are shown in the table below.

As can be seen from Fig. 24 and Table 1, the phase distribution of VPAR-PSI has a smaller envelope (mean envelope reduction of 1.4202λ), smaller RMS and standard deviation (the values decreased by 0.3515, 0.3067, and the percentage decreases were 59.69%, 59.71% respectively) compared to the PSI technique. As a result, the measurements obtained with VPAR-PSI technique are more accurate, stable and smooth than the traditional PSI technique.
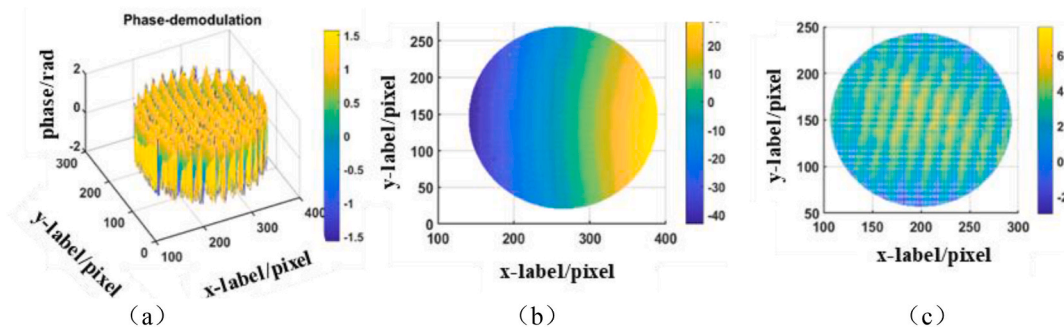
Fig. 21. Measurement results from traditional PSI phase shifting techniques; (a) unwrapped phase map, (b) wrapped phase map, (c) wrapped phase map with tilt removed.
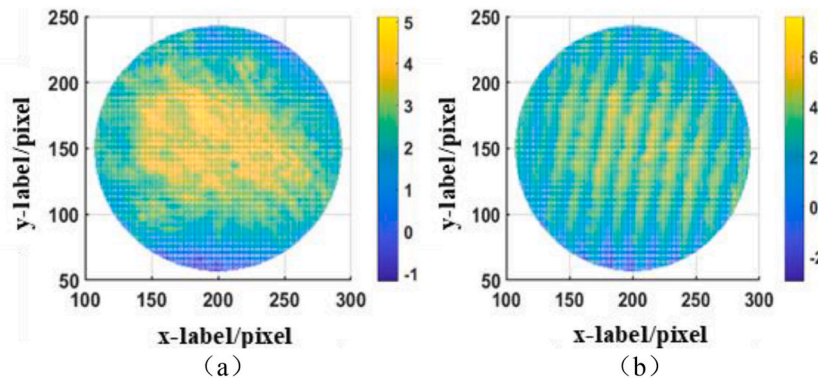

Fig. 22. Comparison of VPAR-PSI and PSI measurements; (a) the results obtained from VPAR-PSI measurements, (b) the results obtained from conventional PSI measurements.
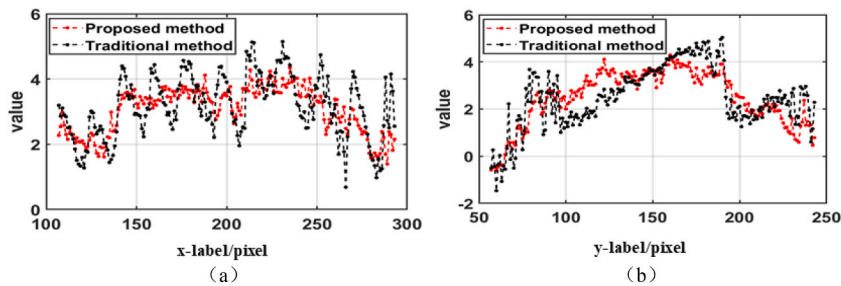

Fig. 23. Comparison of phase distributions obtained from VPAR-PSI and PSI measurements; (a) 150th row of phase distribution; (b) 200th column of phase distribution.
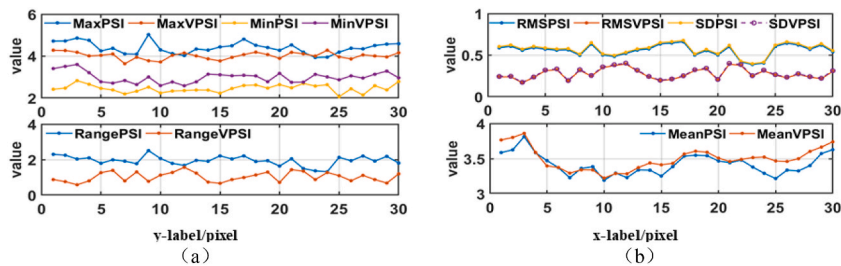

Fig. 24. Comparison of results from VPAR-PSI and PSI techniques; (a) Fig. 23 (a) rows 135–165, columns 185–215 data analysis results; (b) Fig. 23 (b) rows 135–165, columns 185–215 data analysis results.

Table 1

Mean values of the parameters in Fig. 24.

	Maximum values	Minimum values	envelope values	mean values	standard deviation	RMS
PSI	4.7170λ	2.4209λ	2.2961λ	3.5874λ	0.5888λ	0.6041λ
VPAR-PSI	4.2822λ	3.4063λ	0.8759λ	3.7654λ	0.2373λ	0.2434λ

5. Discussion

In order to achieve high accuracy measurements of optical lenses, this manuscript proposes a vortex polar axis rotation Phase-Shifting interferometry (VPAR-PSI) measurement method based on the direct introduction of phase shifting quantities by the polar axis rotation of vortex beam. Compared to traditional PSI, the proposed VPAR-PSI not only avoids the phase shift deviation introduced by the traditional phase shifter, but also avoids the problem of non-linearity between the grey level change and phase, thus ultimately achieving an improved resolution of phase modulation and accuracy.

When compared to conventional PSI phase shifting techniques, VPAR-PSI uses LC-SLM for the phase shifting operation, so the introduction of the phase shift can achieve a pixel-level phase modulation accuracy in the spatial domain, which means that VPAR-PSI can achieve modulation of the differences between different pixels in an interference image.

As can be seen from the flow chart of VPAR-PSI detection shown in Fig. 3, the measurement using the proposed VPAR-PSI requires an initial phase calibration of the vortex beam to be performed first. However, it should be noted that the initial phase calibration process only needs to be performed once after the standard mirror is selected to obtain the corresponding system error file, and the following measurement process can use the obtained system error file for interpolation operations, without the need to perform the initial phase calibration operation for each measurement. Therefore, the VPAR-PSI application process is very convenient.

In the simulation experiments, the data results in Figs. 6, Figs. 8 and 12 show that the VPAR-PSI proposed in this paper can not only achieve accurate phase shift and phase information demodulation, but also have high phase demodulation accuracy, which initially proves the effectiveness of the VPAR-PSI. Sample measurement experiments in Figs. 16 and 19, data results show that the VPAR-PSI proposed in this paper can be well implemented in the practical application of plane mirror and spherical mirror surface shape measurement, and not only has a very high phase demodulation accuracy, and demodulation results have good reliability. In the VPAR-PSI and PSI comparison experiment experiments, the data results in Figs. 23 and 24 and Table 1 show that the measurement results of the proposed VPAR-PSI technique in this paper are more accurate, stable and smooth compared to the traditional PSI technique.

It is worth noting that this manuscript makes use the LC-SLM to achieve VPAR-PSI measurements, which as an up-and-coming device is currently a hot research topic, and that the measurement accuracy of VPAR-PSI is largely limited by the phase modulation accuracy of the LC-SLM. This means that LC-SLM is expected to achieve more widespread applications in the field of phase shift detection with further research on LC-SLM. In addition, LC-SLM for phase modulation has reached a high level of accuracy, and has a short phase shift time, high efficiency and a certain ability to resist vibration.

6. Conclusion

In order to achieve a higher accuracy phase shift, this manuscript introduces the phase shift directly via the rotation of the polar axis of the vortex beam according to the characteristics of vortex beam. In order to verify the effectiveness of the proposed VPAR-PSI method, a series of experiments including simulation experiments, sample testing experiments, and VPAR-PSI and PSI comparison experiments were conducted. The experimental results show that VPAR-PSI has good measurement accuracy, stability. And the proposed VPAR-PSI method has better phase shift accuracy and higher measurement precision than the traditional PSI grey-scale modulation method.

Author contribution statement

Zhisong Li, Jiaxing Sun, Yu Chen: Conceived and designed the experiments; Performed the experiments; Analysed and interpreted the data; Contributed reagents, materials, analysis tools or data; Wrote the paper. Xiao Xua, Honglei Hu: Performed the experiments; Analysed and interpreted the data; Contributed reagents, materials, analysis tools or data; Wrote the paper.

Data availability statement

Data included in article/supp. material/referenced in article.

Additional information

No additional information is available for this paper.

Declaration of competing interest

The authors have no interests to declare.

References

[1] J.H. Bruning, D.R. Herriott, J.E. Gallagher, D.P. Rosenfeld, D.J. Brancaccio, Digital wavefront measuring interferometer for testing optical surfaces and lenses, Appl. Opt. 13 (11) (1974) 2693–2703.
[2] P. Picart, J.C. Pascal, J.M. Bertheau, Systematic errors of phase-shifting speckle interferometry, Appl. Opt. 40 (13) (2001) 2107–2116.
[3] G.Q. Gu, K.F. Wang, Study of phase-shifting techniques in digital speckle pattern interferometry for deformation measurement, Aip Conf. Am. Inst. Phys. 1236 (1) (2010) 57–61.
[4] V.I. Gushov, V.G. Nechaev, In-plane deformation measurement by digital phase-shifting speckle interferometry, Proc. SPIE-Int. Soc. Opt. Eng. 27 (2) (1996) 235–240.
[5] C.L. Koliopoulos, Phase-shifting techniques applied to unique applications, Proc. SPIE-Int. Soc. Opt. Eng. 2861 (1996) 86–93.
[6] R. N, Sivakumar, Large surface profile measurement with instantaneous phase-shifting interferometry, Opt. Eng. 42 (2) (2003) 367–372.
[7] K. Hibino, B.F. Oreb, D.I. Farrant, K.G. Larkin, Phase-shifting algorithms for nonlinear and spatially nonuniform phase shifts, J. Opt. Soc. Am. A 14 (4) (1998) 918–930.
[8] F. Ratovelomanana, N. Vodjdani, Regeneration improvement in all-optical wavelength converter, based on a mach-zehnder interferometer, by means of phase-shifter section, Electron. Lett. 33 (19) (1997) 1629–1630.
[9] Y. Kotaki, S. Ogita, H. Ishikawa, Wavelength tunable semiconductor lasers, Electron. Commun. Jpn. 74 (2) (2010) 29–38.
[10] Z. Shang, W. Li, M. Dong, L. Duan, 3d shape measurement system based on fringe projection in 4-step phase shifting, J. Appl. Opt. 36 (4) (2015) 584–589.
[11] J. Novak, Five-step phase-shifting algorithms with unknown values of phase shift, Optik - Int. J. Light Electron Opt. 114 (2) (2003) 63–68.
[12] J. Novak, A. Miks, Comparison of multiframe phase-shifting algorithms with unknown value of phase shift. Optical Measurement Systems for Industrial Inspection III, Dept. of Physics, Czech Technical University, Thakurova 7,166 29 Prague 6, Czech Republic 56 (8) (2003) 86–95.
[13] Deck, L. Leslie, Model-based phase shifting interferometry, Appl. Opt. 53 (21) (2014) 4628–4641.
[14] Z. Song, Digital multiple wavelength phase shifting algorithm, Proc. SPIE-Int. Soc. Opt. Eng. (2009) 7432–7442.
[15] W. Niu, L. Zhong, S. Peng, C. Luo, L. Xiaoxu, An improved two-step phase-shifting algorithm based on gram-schmidt orthonormalization, Chin. J. Lasers 42 (6) (2015) 608002–608022.
[16] T. Lei, Simulation of the phase-shift and anti-vibration in wavefront time-domain algorithm, Optical Design & Testing 6834 (1) (2007) 68342A1–68342A9.
[17] K.G. Larkin, B.F. Oreb, Propagation of errors in different phase-shifting algorithms: a special property of the arctangent function, Proc. SPIE 1755 (2011) 219–227.
[18] J. Wang, J.L. Pressesky, Quadrature phase shift interferometer (qpsi) decoding algorithms and error analysis, Proc. SPIE-Int. Soc. Opt. Eng. (2003) 5188–5192.
[19] Z. Yan, G. Hui, T. Jinghui, L. Xiangang, H. Minghui, Orbital angular momentum generation via a spiral phase microsphere, Opt Lett. 43 (1) (2018) 34–37.
[20] Ruchi, P. Senthilkumaran, S.K. Pal, Corrigendum to "phase Singularities to Polarization Singularities, Hindawi Limited, 2021.
[21] Y. Shen, Optical vortices 30 years on: OAM manipulation from topological charge to multiple singularities, Light Sci. Appl. 90 (8) (2019) 60–71.
[22] Xinyao, Qian Hu, Zhao, Panpan, Yu, et al., Dynamic shaping of orbital-angular-momentum beams for information encoding, Opt Express 26 (2) (2018) 1796–1808.
[23] J. Wang, Wuhan National Laboratory for Optoelectronics, Information, O. E., Huazhong University of Science and Technology, Advances in communications using optical vortices, Photon. Res. 5 (4) (2016) 14–28.
[24] W. Wei, K. Mahdjoubi, C. Brousseau, O. Emile, Generation of oam waves with circular phase shifter and array of patch antennas, Electron. Lett. 51 (6) (2015) 442–443.
[25] Y. Xu, L. Guo, M. Cheng, J. Li, Controlling abruptly autofocusing vortex beams to mitigate crosstalk and vortex splitting in free-space optical communication, Opt Express 26 (10) (2018) 12605–12619.
[26] S. Fu, S. Zhang, T. Wang, C. Gao, Measurement of orbital angular momentum spectra of multiplexing optical vortices, Opt Express 24 (6) (2016) 6240–6248.
[27] A.D. Errico, Measuring the complex orbital angular momentumspectrum and spatial mode decomposition of structured light beams, Optica 11 (4) (2017) 1350–1357.
[28] S. Khonina, V. Podlipnov, S. Karpeev, A. Ustinov, S. Volotovsky, S. Ganchevskaya, Spectral control of the orbital angular momentum of a laser beam based on 3d properties of spiral phase plates fabricated for an infrared wavelength, Opt Express 28 (12) (2020) 18407–18417.
[29] L.A. Shaw, C.M. Spadaccini, J.B. Hopkins, Scanning holographic optical tweezers, Opt Lett. 42 (15) (2017) 2862–2865.
[30] S. Bernet, A. Jesacher, S. Fürhapter, C. Maurer, M. Ritsch-Marte, Quantitative imaging of complex samples by spiral phase contrast microscopy, Opt Express 14 (9) (2006) 3792–3805.
[31] M. Lavery, Detection of a spinning object using light's orbital angular momentum, Science 341 (6151) (2013) 1175. -1175.
[32] I. Fujimoto, S. Sato, M.Y. Kim, S. Ando, Optical vortex beams for optical displacement measurements in a surveying field, Meas. Sci. Technol. 22 (10) (2011) 1616–1630.
[33] V.V. Kotlyar, A.A. Kovalev, R.V. Skidanov, S.N. Khonina, V.A. Soïfer, Simple optical vortices formed by a spiral phase plate, J. Opt. Technol. 74 (10) (2007) 686–693.
[34] Z. Zhigang, D. Fengliang, Qian Kemao, et al., Real-time phase measurement of optical vortices based on pixelated micropolarizer array, Opt Express 23 (16) (2015) 20521–20528.
[35] C.S. Guo, X. Cheng, X.Y. Ren, J.P. Ding, H.T. Wang, Optical vortex phase-shifting digital holography, Opt Express 12 (21) (2004) 5166–5171.
[36] B. Sokolenko, D. Poletaev, S. Halilov, Phase shifting profilometry with optical vortices, J. Phys. Conf. 917 (6) (2017), 062047.
[37] H. Sun, X. Wang, P. Sun, In-plane displacement measurement using optical vortex phase shifting, Appl. Opt. 55 (21) (2016) 5610–5613.
[38] X. Zhang, J. Zhang, Y. Zhang, D. Liu, J. Zhu, Phase-shifting image-plane digital holography with elliptical vortex sieve, Opt Laser. Technol. 115 (2019) 359–363.
[39] W.P. Wang, S.J. Huang, Y. Chen, J.W. Wang, C. Yan, Three-dimensional refractive index measurement of special optical fiber based on optical vortex phase-shifting digital holographic microscopy, Opt. Eng. 58 (3) (2019), 034108, 1-034108.6.
[40] J. Masajada, M. Leniec, E. Jankowska, H. Thienpont, V. Gomez, Deep microstructure topography characterization with optical vortex interferometer, Opt Express 16 (23) (2008) 19179–19191.
[41] A. Serrano-Trujillo, M.E. Anderson, Surface profilometry using vortex beams generated with a spatial light modulator, Opt Commun. 427 (2018) 557–562.
[42] W. FroCzek, A. PopioEk-Masajada, J. Masajada, Phase shifting technique for vortex points localization in optical vortex interferometer, Int. Soc. Optics Photon. 43 (7) (2008) 1219–1224.

[43] D. Zhao, C. Jia, Y. Ma, X. Yang, B. Zhang, W. Chu, High-accuracy surface profile measurement based on the vortex phase-shifting interferometry, Int. J. Opt. 60 (5) (2021) 520–534.

[44] Stephan, Reichelt, Spatially resolved phase-response calibration of liquid-crystal-based spatial light modulators, Appl. Opt. 52 (12) (2013) 2610–2618.

[45] H.V. Brug, Phase-step calibration for phase-stepped interferometry, Appl. Opt. 38 (16) (1999) 3549–3555.